

Vibrational dynamics of anatase TiO₂: Polarized Raman spectroscopy and *ab initio* calculations

M. Giarola, A. Sanson, F. Monti, and G. Mariotto*

Dipartimento di Informatica, Università degli Studi di Verona, Strada Le Grazie 15, I-37134 Verona, Italy

M. Bettinelli

Dipartimento di Biotecnologie, Università degli Studi di Verona and INSTM, UdR Verona, Strada Le Grazie 15, I-37134 Verona, Italy

A. Speghini

DiSTeMeV, Università degli Studi di Verona and INSTM, UdR Verona, Via della Pieve 70, San Floriano, I-37029 Verona, Italy

G. Salviulo

Dipartimento di Geoscienze, Università degli Studi di Padova, Via Giotto 1, I-35137 Padova, Italy

(Received 23 December 2009; revised manuscript received 13 April 2010; published 24 May 2010)

Vibrational properties of anatase titanium dioxide single crystal are thoroughly investigated by means both of experimental and theoretical approaches. Polarized Raman-scattering experiments were carried out at room temperature in backscattering geometry on a microcrystalline anatase sample under different crystal orientations set by a micromanipulator. All the independent components of the polarizability tensor were separately obtained. In particular, it was possible to evidence, in turn, the different components of the A_{1g} mode, thus unambiguously determining its peak wave number, and then, definitively resolve and identify the A_{1g} and B_{1g} modes of anatase. Moreover, *ab initio* calculations based on density-functional perturbation theory within the generalized gradient approximation have been performed to evaluate infrared (IR) and Raman modes, dielectric tensors, Born effective charges and TO-LO splitting of the IR modes. The agreement between computational and experimental results is much better than the one achieved in previous computational works.

DOI: [10.1103/PhysRevB.81.174305](https://doi.org/10.1103/PhysRevB.81.174305)

PACS number(s): 78.30.-j

I. INTRODUCTION

Titanium dioxide (TiO₂), because of its moderate price, chemical stability and nontoxicity, has been extensively studied for its technological applications, including photocatalysis, optical coatings and optoelectronic devices, but also for its wide interest from a basic research point of view.¹⁻⁴ In fact, titanium dioxide is an insulator, with a band gap of about 3.0 eV,⁵ but, as far as its electrical conductivity is concerned, it can be considered a wide-gap semiconductor due to either the nonstoichiometric effects of incorporated dopant elements or to generation of oxygen vacancies and/or Ti interstitials in the pure material. While neither of these approaches substantially impact the band gap, there is an active research effort to find a dopant which will lower the band gap of TiO₂ into the visible spectrum for efficient photocatalysis with sunlight. In addition, this material shows very interesting properties for surface chemistry applications.⁶

TiO₂ exists in nature in three different crystal structures, i.e., anatase, rutile, and brookite. Among them, the rutile phase, which is the most common and stable form of titanium dioxide,⁷ has been extensively studied since the middle of the last century, even with specific concern to its vibrational properties.⁸⁻¹⁰ On the other hand, the anatase phase has attracted much attention in the last decades due to its widespread use in photocatalysis, photochemical solar cells, optoelectronic devices, and chemical sensors.¹¹⁻¹³ In particular, nanocrystalline anatase aroused strong interest for its physical-chemical properties, as opposed to bulk anatase,¹⁴ and, recently, it has also been shown to be a suitable host for luminescent lanthanide ions.¹⁵

Although many experimental and theoretical studies have been conducted on the anatase phase, its vibrational dynamics properties are not yet fully clarified. In fact, several papers have reported the vibrational spectra of nanocrystalline TiO₂ anatase,¹⁶⁻¹⁹ but only a few papers have dealt with the vibrational spectra of anatase single crystals.²⁰⁻²² The reason of this scarce activity may be due to the difficulty to synthesize good-quality single crystals, large enough to measure the related physical properties.^{23,24} In addition, some assignments of the Raman bands reported in the literature for crystalline anatase TiO₂ are contradictory.^{20,21} Nevertheless, the conclusions reported in the seminal paper by Ohsaka *et al.*,²¹ who neither did observe at room temperature any Raman scattering related to the A_{1g} mode nor were able to unambiguously identify the A_{1g} mode in their low-temperature Raman spectrum, are currently used by Raman spectroscopists to recognize the anatase phase of TiO₂, without taking care of the consistency of their results.

In order to definitively overcome the existing ambiguities about the assignment of the Raman scattering of anatase TiO₂, it is mandatory to perform more accurate vibrational dynamics studies, by combining high-quality polarized Raman-scattering experiments with theoretical simulations on crystalline anatase. In this work, the results of an integrated vibrational dynamics study on single-crystal anatase TiO₂, consisting of highly polarized Raman-scattering measurements and of *ab initio* calculations, are reported and discussed. Through a microsampling approach the Raman-active modes with A_{1g} and B_{1g} symmetry have been definitively discriminated and unambiguously identified. As a second step, *ab initio* calculations, based on density-functional perturbation theory within the generalized gradi-

ent approximation, have been performed to evaluate Raman and infrared (IR) modes, as well as dielectric tensors, Born effective charges and TO-LO splitting of the IR modes. The agreement between our theoretical results and both Raman and IR experimental data is much better than the one achieved in previous computational works. However, the most striking issue of this integrated approach is provided by the innovative experimental approach, which allows to perform very accurate polarized Raman-scattering measurements from a single microcrystal, preliminarily oriented by means of a micromanipulator operated under direct optical inspection and monitored on the screen of a color TV camera.

II. EXPERIMENTAL DETAILS

The sample, used for our investigations, is a natural crystal having the form of a truncated tetragonal bipyramid of volume $0.4 \times 0.5 \times 0.8 \text{ mm}^3$, found in the Maddalena pit near Beura in Val d'Ossola (Italy), associated with small quartz crystals. It consists of several microcrystalline domains, with typical size of about $10 \text{ }\mu\text{m}$, showing, under the microscope inspection, an evident mosaic spread. It belongs to the former Donizetti collection recently acquired by the Mineralogy Museum of the University of Padova (catalog number MMP M7477).

Polarized micro-Raman spectra were collected at room temperature in backscattering geometry from a high optical quality single microcrystal, embedded in the as-received sample, using a triple monochromator (Horiba-Jobin Yvon, model T64000), set in double-subtractive/single configuration, and equipped with holographic gratings having 1800 lines/mm. The spectra were excited by the 514.5 nm line of a mixed Ar-Kr ion gas laser focused onto a spot of $2 \text{ }\mu\text{m}$ in size through the lens of a $10\times$ microscope objective ($\text{NA} = 0.25$) and the power on the sample surface was kept well below 10 mW. Proper orientation of the single microcrystal, of estimated dimensions $10 \times 12 \times 15 \text{ }\mu\text{m}^3$, was achieved using a micromanipulator operated under direct optical inspection and monitored on the screen of a color TV camera interfaced to the objective of the microscope used to focus the laser beam onto the sample. According to Porto's notation,²⁵ we have indicated the scattering configuration as $\bar{k}_i(\bar{E}_i, \bar{E}_s)\bar{k}_s$, where \bar{k}_i and \bar{k}_s are the propagation directions while \bar{E}_i and \bar{E}_s are the polarization directions of the incident and scattered light, respectively. In order to have the same laser power at the sample surface, all spectra were excited without modifying the polarization direction of incident laser radiation, and the polarization setting was ensured by the scattered radiation analyzer, coupled to a scrambler placed at the entrance slit of spectrometer. The scattered radiation, filtered by the fore double monochromator, was detected at the spectrograph output by a charge-coupled-device (CCD) detector, with 1024×256 pixels, cooled by liquid nitrogen. The spectral resolution was better than $0.6 \text{ cm}^{-1}/\text{pixel}$ while an accurate wave-number calibration of the spectrometer was achieved based on the emission lines of a Ne spectral lamp.

Repeated micro-Raman measurements were carried out under the same experimental conditions from different points

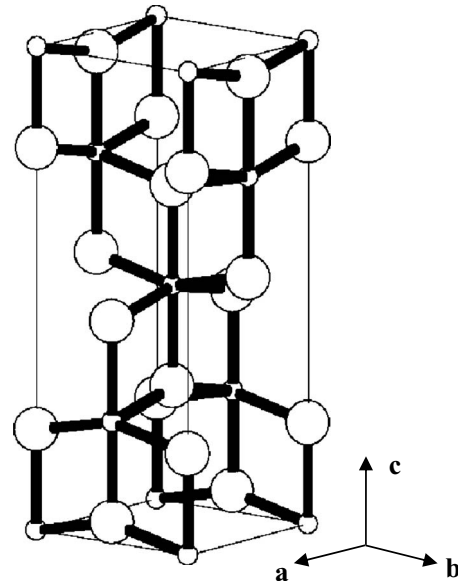


FIG. 1. Crystal structure of anatase phase. Big and small circles denote oxygen and titanium atoms, respectively.

of the investigated microcrystal and the spectra showed a very good reproducibility. No detectable Raman scattering from TiO_2 crystalline phases other than anatase was observed in our polycrystalline sample through systematic measurements carried out from different microdomains displaced some tens of microns each other. Likewise, no Raman scattering was detected from the natural impurities present in our sample by means of this systematic inspection. In fact, natural crystals of anatase are known to contain small amounts of Fe and Sn (Ref. 26) impurities but the related Raman signals were not detectable in our case. Moreover, the presence of luminescent impurities was also ruled out by recording the luminescence spectra from several sample regions under excitation at different wavelengths. Finally, the amount of the mosaic spread (i.e., orientational misalignment of the microcrystalline domains inside the investigated natural sample) was inferred by comparing the intensity of the leaking Raman modes observed under the same experimental conditions in the polarized spectra recorded from several pairs of adjacent microcrystals. According to this procedure, the mosaic spread was then considered remarkable when the spill-over intensity of a forbidden mode was higher than one tenth of that observed for the same mode in the proper polarization setting in which it became allowed. The recorded spectra were processed to remove artifacts due to cosmic rays, while the luminescence background, consisting of a flat and structureless background of very weak intensity underlying the overall Raman spectrum, was subtracted before starting the analysis of the experimental data.

III. POLARIZED RAMAN SPECTRA

The crystallographic structure of anatase is tetragonal with the space group $D_{4h}^{19}(I4_1/amd)$, number 141 in the standard listing. The primitive cell contains two TiO_2 formula units (six atoms). Its structure is shown in Fig. 1: the c axis

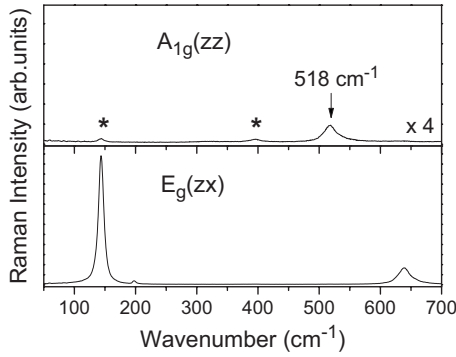


FIG. 2. Room-temperature polarized Raman spectra obtained in backscattering geometry with the electric field vector of the incident light parallel to the c axis of the inspected microcrystal. In the top panel the scale is magnified four times. The stars (*) label the spill-over modes.

is vertical, a and b axes define the basal plane, large and small circles denote O and Ti atoms, respectively.

On the basis of the factor group analysis, 15 optical modes of anatase at the Γ point of the Brillouin zone are expected, with the following irreducible representation of the normal vibrational modes:

$$1A_{1g} + 1A_{2u} + 2B_{1g} + 1B_{2u} + 3E_g + 2E_u. \quad (1)$$

Six modes, i.e., the A_{1g} , $2B_{1g}$, and $3E_g$ are Raman active, whereas the three modes A_{2u} and $2E_u$ are IR active. The mode B_{2u} is silent. Corresponding to each Raman-active mode of anatase, there is a scattering tensor α having a distinctive symmetry, i.e.,²⁷

$$\alpha(A_{1g}) = \begin{pmatrix} a & 0 & 0 \\ 0 & a & 0 \\ 0 & 0 & b \end{pmatrix}, \quad (2)$$

$$\alpha(B_{1g}) = \begin{pmatrix} c & 0 & 0 \\ 0 & -c & 0 \\ 0 & 0 & 0 \end{pmatrix}, \quad (3)$$

$$\alpha(E_g) = \begin{pmatrix} 0 & 0 & d \\ 0 & 0 & d \\ d & d & 0 \end{pmatrix}. \quad (4)$$

To examine experimentally a given component α_{ij} one merely arranges the scattering experiment in such a way that the incident light is polarized in the “ i ” direction while only the scattered light having “ j ” polarization is observed. As Fig. 1 suggests, the crystal structure of anatase TiO₂ is uniaxial. Thus, the determination of the c axis (z direction) may be conveniently done optically as well as by the use of x rays. In our case, we were able to determine this direction in the TiO₂ microcrystal selected for its high optical quality. The related polarized Raman spectra, carried out in backscattering geometry, are reported in Fig. 2, where z , x indicate a set of two orthogonal directions: z is parallel to crystallographic c axis while x belongs to basal (a, b) plane. The

two panels of this figure show the α_{zz} (top) and the α_{zx} (bottom) components, related to the A_{1g} and E_g modes, respectively.

The α_{zz} spectrum exhibits a well shaped and symmetric peak at 518 cm^{-1} , which therefore definitely fixes the wave number of the A_{1g} mode of anatase TiO₂. In spite of its weak intensity, this peak provides the first room-temperature observation of the zz component of A_{1g} mode, which was not found by Ohsaka *et al.*,²¹ neither at room temperature nor at 73 K. In this regard, we believe that Ohsaka *et al.*²¹ were not able to observe it in their α_{xx} Raman spectra due to improper crystal orientation with respect to the electric field of the incident laser beam. On the other hand, they were unable to observe it in their α_{zz} spectrum any Raman band which could be unambiguously assigned to the A_{1g} mode, due to the lower sensitivity of their detection system based on single channel (photomultiplier tube) detection, which does not allow to obtain an optimal signal-to-noise ratio for intrinsically weak signals, as it occurs for the zz component of the A_{1g} mode of anatase. In contrast, we succeeded in observing the zz component of the A_{1g} mode because of the high sensitivity of multichannel (CCD) detection and also, of the nearly perfect alignment of the electric field of the incident light along the crystallographic c axis, achieved thanks to the micromanipulator used to orientate our sample.

Differently from α_{zz} spectrum, the α_{zx} spectrum shows a remarkable scattering intensity for all the E_g modes peaked at about 143 cm^{-1} , 198 cm^{-1} , and 639 cm^{-1} , respectively, although they have quite different relative intensity. The scattering intensity is particularly strong for the E_g mode peaked at about 143 cm^{-1} , which turns out to be by far the strongest Raman peak of anatase TiO₂.

Regardless to their intensity, both the α_{zz} and the α_{zx} polarized spectra suggest that a nearly perfect alignment of the electric field vector of the incident light along the c axis of the inspected microcrystal was achieved during the measurements. In fact, no appreciable spill over of forbidden modes is displayed by α_{zx} spectrum, while it becomes slightly more evident in α_{zz} spectrum, but without any effect on the assignment above.

On the other hand, proper determination of the a and b axes (i.e., the basal x - y plane orientation) by optical approach is sometimes difficult. Improper sample orientation in the basal x - y plane complicates the interpretation of Raman data. Thus, for a D_{4h} crystal an orientational mismatch in the basal x - y plane prevents the selection of spectra with pure A_{1g} or B_{1g} character and can result in ambiguous or wrong assignment of the A_{1g} and B_{1g} phonons, as found in the literature.²¹ However, in order to fully resolve and discriminate the A_{1g} or B_{1g} modes, it is necessary to control the exact orientation of the polarization vector with respect to the crystallographic axis a (or b). We have verified that, when the sample was rotated around its c axis, the intensities of the A_{1g} and B_{1g} bands varied differently, so that, when the proper alignment was matched, the observed Raman spectrum showed a very pure symmetry character, i.e., A_{1g} or B_{1g} symmetry. In fact, upon sample rotation of an angle θ around the c axis, the components α_{XX} and α_{XY} of the Raman tensor, measured in the laboratory coordinate system and referred to its X and Y axes, can be expressed in terms of the compo-

nents α_{xx} , α_{yy} , and α_{xy} of the same Raman tensor in the intrinsic coordinate system, built up on the basal crystal axes x and y , as follows:

$$\alpha_{XX} = (\cos^2 \theta) \alpha_{xx} + (\sin^2 \theta) \alpha_{yy} + (2 \sin \theta \cos \theta) \alpha_{xy} \quad (5)$$

and

$$\alpha_{XY} = (\sin \theta \cos \theta) \alpha_{xx} - (\cos \theta \sin \theta) \alpha_{yy} + (\sin^2 \theta - \cos^2 \theta) \alpha_{xy}, \quad (6)$$

where we have assumed $\alpha_{xy} = \alpha_{yx}$, since the polarizability tensor α is symmetric. Let us now consider the specific form of the scattering tensor corresponding to A_{1g} and B_{1g} Raman-active modes of anatase TiO_2 ,²⁷ in order to derive the intensity of these Raman modes expected under the two polarization settings: XX (parallel) and XY (crossed) polarization, respectively.

In the XX (parallel) polarization setting, $\alpha_{xx} = \alpha_{yy}$ and $\alpha_{xy} = 0$ for the A_{1g} mode, and the polarizability component $\alpha_{XX}(A_{1g})$ is unchanged upon rotation. Therefore, the A_{1g} mode will be observed with the same intensity for any value of the rotation angle θ . On the other hand, in the same parallel polarization setting, $\alpha_{xx} = -\alpha_{yy}$ and $\alpha_{xy} = 0$ for a B_{1g} mode, and the polarizability component $\alpha_{XX}(B_{1g})$ varies according to $\cos(2\theta)\alpha_{xx}$. As a consequence, a B_{1g} mode will show the maximum intensity for $\theta = 0^\circ$ or 90° and will be zero for $\theta = 45^\circ$. In contrast, in the XY (crossed) polarization setting, the intensity of A_{1g} mode will always be zero, since $\alpha_{XY}(A_{1g}) = 0$, independently of the angle θ , while the intensity of a B_{1g} mode, for which $\alpha_{XY}(B_{1g}) = \sin(2\theta)\alpha_{xx}$, will turn out to be maximum when $\theta = 45^\circ$ and zero for $\theta = 0^\circ$. According to Eq. (4), the intensity of the E_g modes will be zero for any value of the angle θ , in both XX and XY polarizations.

On the basis of the above predictions and adopting the backscattering geometry with the direction of incident and scattered radiation parallel to c axis of the inspected microcrystal, we succeeded in properly orienting our microcrystal in the basal x - y plane in order to discriminate pure A_{1g} mode when $\theta = 45^\circ$ or both $A_{1g} + B_{1g}$ modes when $\theta = 0^\circ$. The polarized Raman spectra measured in this backscattering configuration at room temperature under the different polarization and orientation settings are shown in Fig. 3. They correspond to distinctive symmetries of the TiO_2 anatase vibrational modes associated with polarizability components belonging to the basal x - y plane.

The spectrum displayed in the panel (a) of Fig. 3 consists of a single, slightly asymmetric peak at 518 cm^{-1} , which is the ‘‘carbon copy’’ the α_{zz} spectrum of Fig. 2, although stronger in intensity, and therefore has to be identified as the A_{1g} mode. The purity degree of this A_{1g} spectrum suggests a nearly perfect matching of the crystal orientation (corresponding to a rotation angle $\theta = 45^\circ$ with respect to the crystallographic axis a or b) with the direction of the electric field of the incident laser radiation. Moreover, the negligible spill over of the forbidden E_g mode at 143 cm^{-1} testifies for the excellent alignment of the c axis of the microcrystal under inspection along the direction of the optical axis of our focusing system. Finally, the faint band centered at about 320 cm^{-1} should be assigned to second-order scattering,

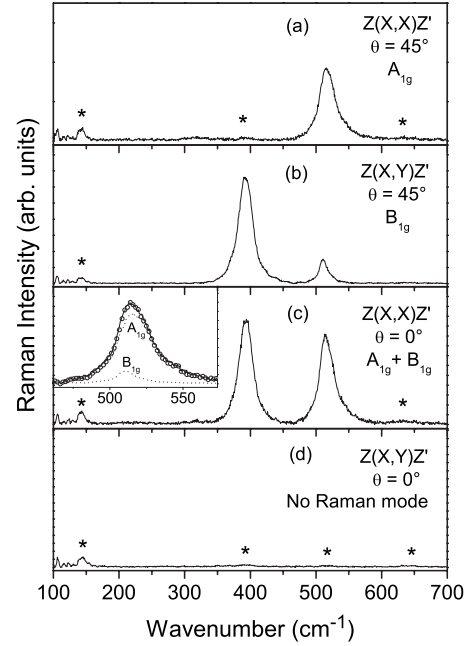


FIG. 3. Room-temperature polarized Raman spectra obtained in backscattering geometry (with $Z' = -Z$) for different polarization and orientation setting (see text). The inset of panel (c) shows, in the spectral region of interest, the overlay (continuous line) of the two A_{1g} and B_{1g} peaks (dotted lines) with the experimental spectrum (open circles). The stars (*) label the spill-over modes. Note the very faint intensity of the forbidden modes in panel (a). The arrows at about 320 cm^{-1} refer to the A_{1g} component of the second-order scattering. Finally, the weak spectral features occurring in the region between 100 and 140 cm^{-1} are due to rotational modes of the air.

which always shows an A_{1g} symmetry component, as already observed by Ohsaka *et al.*²¹ in the same XX polarization.

As for the spectrum shown in the intermediate panel (b) measured in XY (crossed) polarization for the same microcrystal orientation (i.e., $\theta = 45^\circ$), two distinct, slightly asymmetric peaks are observed, the stronger one at about 395 cm^{-1} , and the weaker one at about 512 cm^{-1} , besides a very weak feature at about 143 cm^{-1} . According to the Eq. (6) these peaks have to be assigned to the two expected B_{1g} modes since the intensity of A_{1g} mode in crossed polarization is always zero independently of the crystal orientation in the basal x - y plane. As for the minor feature at 143 cm^{-1} , originating from the spill over of the forbidden E_g mode, it deserves the same considerations already made for the spectrum observed in the XX polarization.

The spectrum displayed in the panel (c), measured in parallel XX polarization when the sample orientation matched the crystallographic a axis (i.e., $\theta = 0^\circ$), consists of two major peaks, and two minor features, one of which, peaked at about 143 cm^{-1} , originates from the spill over of the E_g mode, while the faint band centered at about 320 cm^{-1} represents the A_{1g} symmetry component of the second-order scattering. As for the two major peaks, the stronger one, slightly asymmetric, occurs at about 395 cm^{-1} , while the other one is observed to peak at about 515 cm^{-1} , with a more pronounced asymmetry on the side of higher wave numbers

with respect to the maximum. A very similar spectrum was observed in the same polarization by Ohsaka *et al.*,²¹ who properly assigned the band at 399 cm⁻¹ to a B_{1g} mode, and discussed the band at 516 cm⁻¹ in terms of a doublet resulting from A_{1g} and B_{1g} modes, but were unable to unambiguously assign these two component modes. This bottleneck can be now definitively overcome and the correct assignment of the two different component modes can be done. In fact, on the basis of the above predictions, the overall spectrum should consist of either the A_{1g} mode, whose intensity does not depend on the sample rotation around its *c* axis, or of the two B_{1g} modes, which are expected to have maximum intensity just at $\theta=0^\circ$. Thus the superposition of the “nearly” degenerate modes A_{1g} (at 518 cm⁻¹) and B_{1g} (at 512 cm⁻¹) turns out into an apparent single (unresolved) asymmetric band peaked at 515 cm⁻¹ as observed in panel (c). This situation is clearly evidenced in the inset of the panel (c), where the overlay (continuous line) of the properly weighted A_{1g} and B_{1g} peaks (dotted lines), taken from the panel (a) and (b), respectively, turns out to fit well the experimental spectrum (open circles).

In contrast, the spectrum shown in panel (d), recorded in crossed XY polarization, does not display any appreciable spectral contribution neither from the A_{1g} mode nor from B_{1g} modes. This finding perfectly fits with the above derived predictions for $\theta=0^\circ$, henceforth strengthening our conviction about the sharp crystal orientation along the crystallographic *a* axis achieved during the measurements of spectra of both the panels (c) and (d). We should stress here this crucial point. In fact, the substantial absence of any Raman intensity in the spectrum displayed in panel (d) provides the definitive proof of the nearly perfect orientation of the inspected microcrystal parallel to the direction of the electric field of the incident laser radiation, this achievement being obtained thanks to the micromanipulator. Finally, as already pointed out, the weak peak at 143 cm⁻¹, due to E_g mode spill over and present in both the panels (c) and (d), results from a minor misalignment of *c* axis of the microcrystal under inspection with respect to optical axis of the focusing system. Although the polarization of the spectra recorded under the different experimental configurations cannot be fully pure due to the impossibility to perfectly orient the sample, nevertheless the polarization degree of the resolved peaks in the different configurations does not prevent the definitive determination of the distinctive symmetry of the Raman-active modes selected by a proper sample orientations.

IV. AB INITIO CALCULATIONS

Ab initio calculations, based on density-functional perturbation theory within the generalized gradient approximation, have been performed in order to calculate the Raman and IR modes of anatase, as well as the static and high-frequency dielectric tensors, the Born effective charges and TO-LO splitting of the IR modes. Similar *ab initio* simulations were carried out by Mikami *et al.*²⁸ but, differently from the present paper, the calculations were performed in local-density approximation (LDA), with different exchange-correlation functionals and basis sets. More important, our

TABLE I. Born effective charge tensors in anatase phase. Column (a) refer to this work, column (b) to the values calculated by Mikami *et al.* (Ref. 28). The directions *xx*, *yy*, and *zz* are along *a*, *b*, and *c* in the conventional cell, respectively.

	Ti (a)	Ti (b)	O (a)	O (b)
Z_{xx}^*	+6.592	+6.678	-1.266	-1.161
Z_{yy}^*	+6.592	+6.678	-5.334	-5.517
Z_{zz}^*	+5.796	+5.713	-2.883	-2.856

theoretical calculations show a better agreement with experimental data.

The CRYSTAL06 program²⁹ has been used for the present calculations. CRYSTAL is a periodic *ab initio* program that uses a Gaussian-type basis set to represent the crystalline orbitals. Details on basis sets and computational parameters can be found at the CRYSTAL website,³⁰ where input and output files are also available. In the present case, all-electron basis sets have been adopted, with 86–51G* (Refs. 31 and 32) and 8–411d1 (Ref. 33) contractions (one *s*, three *sp*, and one *d* shell) for titanium and oxygen atoms, respectively. Pure density-functional theory calculations have been performed using Becke exchange and Lee-Yang-Parr correlation functionals.^{34,35} Other exchange-correlation functionals have been tested but with worse results. The level of accuracy in evaluating Coulomb and exchange series is controlled by five parameters, for which standard values have been used (6 6 6 6 12). Self-consistent-field convergence thresholds of 10⁻⁷ hartree for both eigenvalues and total energies have been adopted in order to ensure good convergence. Brillouin-zone integration is computed with a Monkhorst-Pack shrinking factor^{36,37} equal to 8. The calculation of the vibrational frequencies is performed within the harmonic approximation. At the Γ point, the frequencies have been obtained by diagonalizing the mass-weight Hessian matrix, whose (*i*, *j*) element is defined as $W_{ij}=H_{ij}/\sqrt{M_i M_j}$, where *M_i* and *M_j* are the masses of the atoms associated with the *i* and *j* coordinates, respectively. For a more complete description of the method and details on computational aspects, see Refs. 38 and 39.

The geometry optimization gives the cell parameters *a* = *b* = 3.8117 Å, *c* = 9.7136 Å, and *c/a* = 2.548, which differ from the experimental values⁴⁰ by about 0.6%, 2.0%, and 1.3%, respectively. These cell parameters have been used in the calculations reported below.

The calculated Born effective charge tensors are displayed in Table I, wherein they are diagonalized with two independent component for Ti atoms, three independent component for O atoms. Our calculations are compared with the values calculated by Mikami *et al.*,²⁸ which substantially confirm our results. Titanium in anatase displays an effective charge which is larger than the nominal ionic charge (+4) of the Ti ion. On the other hand, oxygen atoms display a strong anisotropy of the Born effective charge; the *xx* component is much smaller than the others and smaller than the nominal ionic charge (-2). A similar behavior was found in the rutile phase, owing to the similar local structure of titanium and oxygen sites.^{41,42}

The most interesting result of this computational study is the wave number determination of the optical modes, includ-

TABLE II. Observed and calculated wave numbers of anatase crystal (in per centimeter) at the Γ point. Columns (a) and (c) refer to the present work, (b) to Ref. 28, (d) to Ref. 20, (e) to Ref. 21, and (f) to Ref. 22. The three indices $|\overline{\Delta}|$, $|\overline{\Delta}_r|\%$, and $|\Delta_{\max}|$ (see text) are listed at the end of table.

Raman modes	Theory (a)	Theory (b)	Expt. (c)	Expt. (d)	Expt. (e)
$E_g(1)$	156.7	145.6	143	144	144
$E_g(2)$	190.5	171.1	198	197	197
$B_{1g}(1)$	380.5	398.4	395	400	399
$B_{1g}(2)$	520.2	518.4	512	515	519 ^a
A_{1g}	518.6	535.9	518	519	513 ^a
$E_g(3)$	640.8	662.1	639	640	639
Infrared modes	Theory (a)	Theory (b)	Expt. (f)		
$E_u(1)$ (TO)	262.5	248.6	262		
$E_u(1)$ (LO)	354.5	340.6	366		
$A_{2u}(1)$ (TO)	333.7	375.3	367		
$A_{2u}(1)$ (LO)	730.5	743.1	755		
$E_u(2)$ (TO)	432.4	479.9	435		
$E_u(2)$ (LO)	879.0	892.2	876		
Silent B_{2u}	542.1	564.6			
$ \overline{\Delta} $	10.1	16.1			
$ \overline{\Delta}_r \%$	2.9	4.2			
$ \Delta_{\max} $	33.3	44.9			

^aFrequencies measured at 73 K.

ing the TO-LO splitting of the infrared modes. The calculated wave numbers and their comparison with the available experimental data²⁰⁻²² as well as with the Raman result of the present work are reported in Table II. The computational results of Mikami *et al.*²⁸ are also reported.

To compute the TO-LO splitting, the dynamic dielectric tensor must be calculated. To this aim, a finite-field perturbation method implemented in CRYSTAL code with the ‘‘sawtooth’’ approach⁴³ has been used. The number of unit cells in the applied field direction was 6, and 40 points were chosen for the Fourier transform. The calculated values of the static (ϵ^0) and high-frequency (ϵ^∞) dielectric tensor are given in Table III. The agreement between the experimental data and our calculated dielectric tensors is very good.

TABLE III. High frequency and static dielectric tensor of anatase phase. Column (a) refer to the values calculated in this work, column (b) to the values calculated by Mikami *et al.* (Ref. 28) in the LDA [the values in parenthesis have been predicted with the scissor technique (Ref. 42)], column (c) to the average of the experimental values reported in Refs. 22 and 44, respectively.

	Theory (a)	Theory (b)	Expt. (c)
$\epsilon_{xx}^\infty = \epsilon_{yy}^\infty$	6.05	7.07(6.00)	6.18
ϵ_{zz}^∞	5.75	6.21(5.39)	5.80
$\epsilon_{xx}^0 = \epsilon_{yy}^0$	45.6	45.9	45.1
ϵ_{zz}^0	27.6	24.4	22.7

The comparison between calculated (ν^{cal}) and experimental (ν^{exp}) wave numbers has been made through three indices defined as follows:

$$|\overline{\Delta}| = \frac{1}{N} \sum_{i=1}^N |\nu_i^{cal} - \nu_i^{exp}|, \quad (7)$$

$$|\overline{\Delta}_r|\% = \frac{100}{N} \sum_{i=1}^N \left| \frac{\nu_i^{cal} - \nu_i^{exp}}{\nu_i^{exp}} \right|, \quad (8)$$

$$|\Delta_{\max}| = \max(|\nu_i^{cal} - \nu_i^{exp}|), \quad (9)$$

where $i=1, \dots, N$ indicates the 12 optical modes (including the LO infrared modes) listed in Table II, $|\overline{\Delta}|$, $|\overline{\Delta}_r|\%$, and $|\Delta_{\max}|$ are the average of the absolute difference, the average of the relative differences (in percentage), and the maximum difference, respectively. We have considered as experimental frequencies ν_i^{exp} the average of the available experimental data, i.e., the average of the columns (c), (d), and (e) of Table II for the Raman modes, column (f) for the infrared modes. The three indices are reported at the end of Table II. For comparison, also the indices related to the frequencies calculated by Mikami *et al.*²⁸ are reported. The indices show a better agreement of our calculations with respect to the frequencies calculated by Mikami *et al.*²⁸

V. CONCLUSIONS

In this work, through a proper polarization analysis, all the active Raman modes of TiO₂ anatase have been selected in turn and assigned in symmetry. Moreover, the two nearly degenerate modes at about 515 cm⁻¹ have been clearly isolated, and the A_{1g} mode definitively identified as the more energetic one, thus supporting the assignment first proposed by Beattie and Gilson.²⁰ Finally, Raman and infrared modes, dielectric tensors, Born effective charges, and TO-LO splitting have been determined using *ab initio* calculations based on density-functional perturbation theory. The agreement between computational and experimental results is much better than the one achieved in previous computational works. As final remark, we should mention that the most promising issue of this of this work is provided by the innovative ex-

perimental approach, which allows to carry out very thorough polarized Raman-scattering experiments on a single microcrystal, preliminarily oriented by means of a micromanipulator operated under direct optical inspection on a color TV camera, interfaced to the same microscope objective used to focus the laser beam onto the sample. In fact, this approach provides a suitable route for further, more accurate studies on an extremely large variety of polycrystalline materials.

ACKNOWLEDGMENTS

The authors are grateful to E. Cazzanelli for the useful discussions and the critical reading of the manuscript. This research was partially funded by the Fondazione Cariverona under contract with the University of Verona.

*Corresponding author; gino.mariotto@univr.it

- ¹M. F. Yan and W. W. Rhodes, in *Grain Boundaries in Semiconductors*, edited by H. J. Leamy, G. E. Pike, and C. H. Seager (North-Holland, New York, 1981).
- ²J. Reintjes and M. B. Schultz, *J. Appl. Phys.* **39**, 5254 (1968).
- ³J. Tauster, S. C. Fung, and R. L. Garten, *J. Am. Chem. Soc.* **100**, 170 (1978).
- ⁴D. J. Dwyer, S. D. Cameron, and J. Gland, *Surf. Sci.* **159**, 430 (1985).
- ⁵L. Kavan, M. Grätzel, S. E. Gilbert, C. Klemenz, and H. J. Scheel, *J. Am. Chem. Soc.* **118**, 6716 (1996).
- ⁶U. Diebold, *Surf. Sci. Rep.* **48**, 53 (2003).
- ⁷T. Sekiya, S. Ohta, S. Kamei, M. Hanakawa, and S. Kurita, *J. Phys. Chem. Solids* **62**, 717 (2001).
- ⁸B. Dayal, *Proc. Indian Acad. Sci., Sect. A* **32A**, 304 (1950).
- ⁹D. M. Eagles, *J. Phys. Chem. Solids* **25**, 1243 (1964).
- ¹⁰S. P. S. Porto, P. A. Fleury, and T. C. Damen, *Phys. Rev.* **154**, 522 (1967).
- ¹¹A. Fujishima and K. Honda, *Nature (London)* **238**, 37 (1972).
- ¹²M. Grätzel, *Comments Inorg. Chem.* **12**, 93 (1991).
- ¹³K. I. Hadjiivanov and D. K. Klissurski, *Chem. Soc. Rev.* **25**, 61 (1996).
- ¹⁴H. Gleiter, *Prog. Mater. Sci.* **33**, 223 (1989).
- ¹⁵M. Bettinelli, A. Speghini, D. Falcomer, M. Daldosso, V. Dallacasa, and L. Romanò, *J. Phys.: Condens. Matter* **18**, S2149 (2006).
- ¹⁶V. Swamy, A. Kuznetsov, L. S. Dubrovinsky, R. A. Caruso, D. G. Shchukin, and B. C. Muddle, *Phys. Rev. B* **71**, 184302 (2005).
- ¹⁷W. F. Zhang, Y. L. He, M. S. Zhang, Z. Yin, and Q. Chen, *J. Phys. D* **33**, 912 (2000).
- ¹⁸M. Grujić-Brojčin, M. J. Šćepanović, Z. D. Dohčević-Mitrović, I. Hinić, B. Matović, G. Stanišić, and Z. V. Popović, *J. Phys. D* **38**, 1415 (2005).
- ¹⁹D. Bersani, P. P. Lottici, and X. Z. Ding, *Appl. Phys. Lett.* **72**, 73 (1998).
- ²⁰I. Beattie and T. R. Gilson, *Proc. R. Soc. London, Ser. A* **307**, 407 (1968).
- ²¹T. Ohsaka, F. Izumi, and Y. Fujiki, *J. Raman Spectrosc.* **7**, 321 (1978).
- ²²R. J. Gonzalez, R. Zallen, and H. Berger, *Phys. Rev. B* **55**, 7014 (1997).
- ²³H. Berger, H. Tang, and F. Lévy, *J. Cryst. Growth* **130**, 108 (1993).
- ²⁴D. Das Mulmia, T. Sekiya, N. Kamiya, S. Kurita, Y. Murakami, and T. Kodaira, *J. Phys. Chem. Solids* **65**, 1181 (2004).
- ²⁵T. C. Damen, S. P. S. Porto, and B. Tell, *Phys. Rev.* **142**, 570 (1966).
- ²⁶D. Palanca, H. Berman, and D. Frondel, *Dana's Systems of Mineralogy* (John Wiley, New York, 1963), Vol. 1, p. 583.
- ²⁷R. Loudon, *Adv. Phys.* **13**, 423 (1964).
- ²⁸M. Mikami, S. Nakamura, O. Kitao, and H. Arakawa, *Phys. Rev. B* **66**, 155213 (2002).
- ²⁹R. Dovesi, V. R. Saunders, C. Roetti, R. Orlando, C. M. Zicovich-Wilson, F. Pascale, K. Doll, N. M. Harrison, B. Civalieri, I. J. Bush, P. D'Arco, and M. Llunell, *Crystal06 User's Manual* (Università di Torino, Torino, 2006).
- ³⁰www.crystal.unito.it
- ³¹J. Muscat, Ph.D. thesis, University of Manchester, 1999.
- ³²J. Scaranto and S. Giorgianni, *J. Mol. Struct.: THEOCHEM* **858**, 72 (2008).
- ³³F. Corà, *Mol. Phys.* **103**, 2483 (2005).
- ³⁴A. D. Becke, *Phys. Rev. A* **38**, 3098 (1988).
- ³⁵C. Lee, W. Yang, and R. G. Parr, *Phys. Rev. B* **37**, 785 (1988).
- ³⁶C. Pisani, R. Dovesi, and C. Roetti, *Hartree-Fock ab initio Treatment of Crystalline Systems*, Lecture Notes in Chemistry Vol. 48 (Springer-Verlag, Heidelberg, 1988).
- ³⁷H. Monkhorst and J. Pack, *Phys. Rev. B* **13**, 5188 (1976).
- ³⁸C. M. Zicovich-Wilson, F. Pascale, C. Roetti, V. R. Saunders, R. Orlando, and R. Dovesi, *J. Comput. Chem.* **25**, 1873 (2004).
- ³⁹F. Pascale, C. M. Zicovich-Wilson, F. L. Gejo, B. Civalieri, R. Orlando, and R. Dovesi, *J. Comput. Chem.* **25**, 888 (2004).
- ⁴⁰C. J. Howard, T. M. Sabine, and F. Dickson, *Acta Crystallogr., Sect. B: Struct. Sci.* **47**, 462 (1991).
- ⁴¹C. Lee and X. Gonze, *Phys. Rev. B* **49**, 14730 (1994).
- ⁴²C. Lee, P. Ghosez, and X. Gonze, *Phys. Rev. B* **50**, 13379 (1994).
- ⁴³C. Darrigan, M. Rerat, G. Mallia, and R. Dovesi, *J. Comput. Chem.* **24**, 1305 (2003).
- ⁴⁴*CRC Handbook of Chemistry and Physics on Cd-rom, 2000 Version*, edited by D. R. Lide (CRC Press, Boca Raton, 2000).